ADVANCED FUNCTIONAL MATERIALS
www.afm-journal.de

Unraveling the Morphology-Function Correlation of Mesoporous ZnO Films upon Water Exposure

*Ting Tian, Suo Tu, Ang Xu, Shanshan Yin, Anna Lena Oechsle, Tianxiao Xiao, Apostolos Vagias, Johanna Eichhorn, Jinping Suo, Zhangcan Yang, Sigrid Bernstorff, and Peter Müller-Buschbaum**

Ubiquitous moisture in synthetic conditions and ambient environments can strongly influence the conductivity of ZnO semiconductors via the chemisorption and physisorption of water molecules on the ZnO surface. Such an intrinsically water-sensitive nature will become more evident in mesoporous ZnO films where a large surface area and active sites are created simultaneously. However, fundamental insights underlying water-mediated ZnO surface chemistry and electrical conductivity and the factors affecting them remain ambiguous due to the complexity of ZnO surfaces and the difficulties of in situ characterizations at multi-dimensions. Here, self-assembling diblock copolymers are exploited as structure-directing agents to achieve mesoporous ZnO thin films with highly tailorable structural characteristics ranging from nanomorphologies, over crystalline levels, to defect contents. As verified by theoretical calculations, the presence of oxygen vacancy will facilitate favorable water adsorption and subsequent dissociation on the polar ZnO surfaces. Upon humidity exposure with progressively increased levels, mesoporous ZnO films are revealed to follow an almost positive relationship between adsorption and electrical conductivity but show superior morphological stability. This work not only elucidates the water-governed ZnO surface chemistry but may also promote a comprehensive understanding of the morphology-function relationship on ZnO-based electronics.

1. Introduction

Nanostructured ZnO architectures, distinguished by their morphological richness and intrinsic multifunctionality, have emerged as a flexible and effective platform that can be integrated into interdisciplinary nanotechnologies, ranging from photoelectric conversion, environmental monitoring, and biomedical diagnoses.[1] In particular, introducing mesoporous frameworks into ZnO structures would further broaden the dimension of their practical applications by creating higher surface area, more reaction active sites, and favorable electron/ion/mass transport pathways.[2] Over the past decades, extensive research efforts have been devoted to the fabrication and device assembly of mesoporous ZnO, witnessing the critical role of morphology on final performance.[3] Nevertheless, the underlying mechanisms have been sophisticated due to the interplay between affecting factors,[4] and more comprehensive insights into the

T. Tian, S. Tu, S. Yin, A. L. Oechsle, T. Xiao, P. Müller-Buschbaum
TUM School of Natural Sciences, Department of Physics
Chair for Functional Materials
Technical University of Munich
James-Franck-Str. 1, 85748 Garching, Germany
E-mail: muellerb@ph.tum.de

A. Xu, J. Suo
Key Laboratory of Material Processing and Die and Mould Technology
School of Materials Science and Engineering
Huazhong University of Science and Technology
Wuhan 430074, China

The ORCID identification number(s) for the author(s) of this article can be found under https://doi.org/10.1002/adfm.202311793

© 2023 The Authors. Advanced Functional Materials published by Wiley-VCH GmbH. This is an open access article under the terms of the Creative Commons Attribution License, which permits use, distribution and reproduction in any medium, provided the original work is properly cited.

DOI: 10.1002/adfm.202311793

A. Vagias, P. Müller-Buschbaum
Heinz Maier-Leibnitz Zentrum (MLZ)
Technical University of Munich
Lichtenbergstr. 1, 85748 Garching, Germany

J. Eichhorn
Physics Department
TUM School of Natural Sciences
Technical University of Munich
James-Franck-Str. 1, 85748 Garching, Germany

J. Eichhorn
Walter Schottky Institute
Technical University of Munich
Am Coulombwall 4, 85748 Garching, Germany

Z. Yang
Department of Nuclear Engineering and Technology
School of Energy and Power Engineering
Huazhong University of Science and Technology
Wuhan 430074, China

S. Bernstorff
Elettra-Sincrotrone Trieste S.C.p.A.
AREA Science Park
Strada Statale 14 km 163.5, Basovizza, Trieste 34149, Italy

morphology-property relationships of ZnO-based nanodevices are essential.

Among existing synthetic strategies that afford highly tailorable ZnO morphology, using block copolymers (BCPs) as building blocks offers incomparable advantages, especially in generating regularly arranged pores at a mesoscale (2–50 nm).[5] Based on the rich phase separations via spontaneous self-assembly, a single BCP can achieve a multitude of nanostructures and porous morphologies by simply manipulating the thermodynamic and kinetic factors, which is unattainable by other structure-directing agents.[6] Taking the frequently used amphiphilic BCPs as an instance, the intrinsic incompatibility arising from the chemically dissimilar but covalently connected hydrophobic and hydrophilic moieties would manifest as a repulsive interaction, driving the phase separation into ordered nanostructures with different geometries and dimensions. By selective incorporation of a third phase or mixed phase via a favorable intermolecular interaction such as hydrogen bonding, electrostatic, and van der Waals interactions, this BCP self-assembly concept can be successfully extended to multiple ordered nanostructures including mesoporous materials.[7] In a typical BCP-guided sol–gel synthesis, the hydrophobic segments act as the pore-forming agent, while hydrophilic ones that contain sol–gel precursors define the pore walls, namely, the frameworks surrounding the pores.[8] Even with the same types of BCP as building blocks, the obtained mesoporous ZnO films might deviate from the TiO_2 counterparts, reflecting the morphological complexity and diversity in the BCP-assisted sol–gel systems.[9] As one key issue in wet-chemical synthesis, structural transformation often occurs during the formation or post-treatment processes due to multiple thermodynamic or kinetic factors, thereby hindering the fabrication of mesoporous materials in a reliable and reproducible way. Therefore, an in-depth understanding of the formation pathway is fundamental for achieving a more precise morphology control and consequently realizing tailored functionalities and device performance.

Irrespective of the synthesis routes and fabrication conditions, almost all ZnO surfaces are unavoidably covered by water due to the high surface sensitivity toward ambient moisture, especially for porous ZnO structures attributing to the significantly increased contact area with water vapor exposure. In this context, the ubiquitous water would significantly impact the functionality and durability of a broad spectrum of ZnO-related electronics by modulating the electrical properties via surface adsorption.[10] Although numerous research efforts have been devoted to investigating how water impacts the ZnO conductivities, a simple general rule applicable to all experimental phenomena does not exist to the best of our knowledge. Up to now, the effect of water has been documented to be manifold and elusive, depending not only on the nanoscale morphological features and crystallographic properties but also on the atomic-level defect chemistry. Generally speaking, the water molecules in ambient environments preferentially interact with ZnO solid surface in the form of hydroxylates (OH), which are generated via energetically favorable chemical dissociation.[11] With such strong bonding, OH would be closely attached to the ZnO surfaces and can be only removed by annealing with temperatures higher than 100 °C.[12] Identifying partially hydroxylated ZnO surfaces has deepened the understanding of surface chemistry and close correlations between OH-containing ZnO surfaces and photocatalysis activity or solar cell stability have been elucidated.[13] Following this, a vast number of strategies were explored to exploit/avoid such an effect by promoting/suppressing the hydroxylation of the ZnO surfaces.[14] Besides, these chemically adsorbed OH species would serve as additional adsorption sites for physical adsorption via double hydrogen-bonding networks, leading to a second water monolayer in an energetically degenerate configuration. Due to the dynamic equilibrium between the dissociation and recombination, water molecules introduced on the ZnO surface would switch back and forth between the configurations of OH, $(H_2O)_n$, or coexisted OH + $(H_2O)_n$.[15] Both surface geometry and defect levels are critical in determining the degree of ZnO surface sensitivity and the corresponding extent of water that can be adsorbed.[16] As a type of predominant defect in ZnO, the oxygen vacancy can act as active sites and regulate the surface chemistry by participating in water adsorption. While the surface geometries exert a complex effect, most works so far have concentrated on nonpolar facets and confirmed that water organizes on the surface with partial dissociation within the adsorbed layer, displaying well-organized patterns with half of the surface sites occupied by OH function groups.[17] Due to the high sensitivity but difficulties in constructing surface models for the polar facets, in-depth insights into water adsorption and dissociation on polar ZnO surfaces remain to be further elucidated. Although most ZnO-related works have primarily been dedicated to revealing the effect of water from a specific aspect, few instances exist for more multidimensional investigations, especially in situ monitoring.

In the present work, we fabricate different mesoporous ZnO thin films by exploiting BCPs as structure-directing agents, which are then used as model systems to investigate the impact of the morphology on the water-modulated conductive behaviors. Benefiting from the different inorganic ZnO interconnectivity with the abundant presence of porous frameworks, these thin films are endowed with tailorable structural properties and defect densities. Note that the incorporation of pores is at the sacrifice of the ZnO crystallinity but creates more defect sites, however, no straightforward relationship can be found between them. As the dominant point defect, oxygen vacancy on the ZnO surface would promote water adsorption and subsequent dissociation. The water-impacted conductivity and morphology are explored by monitoring the water adsorption, conductivity changes, and morphology evolutions in situ. Predominantly, the morphology effect is manifested as the grid-like ZnO film demonstrates the fastest water adsorption kinetics and highest humidity sensitivity, mainly due to its higher oxygen vacancy levels and better structural interconnectivity. This sheds light on the water-modulated conductivity of ZnO film, which is expected to pave the way for further morphology control and property manipulation toward next-generation ZnO-based applications.

2. Results and Discussion

2.1. Synthesis and Morphological Characteristics

As for the structure-directing agents, amphiphilic polystyrene-*block*-polyethene oxide (PS-*b*-PEO) and polystyrene-*block*-poly(4-vinyl pyridine) (PS-*b*-P4VP) with different molecular weights are

© 2023 The Authors. Advanced Functional Materials published by Wiley-VCH GmbH

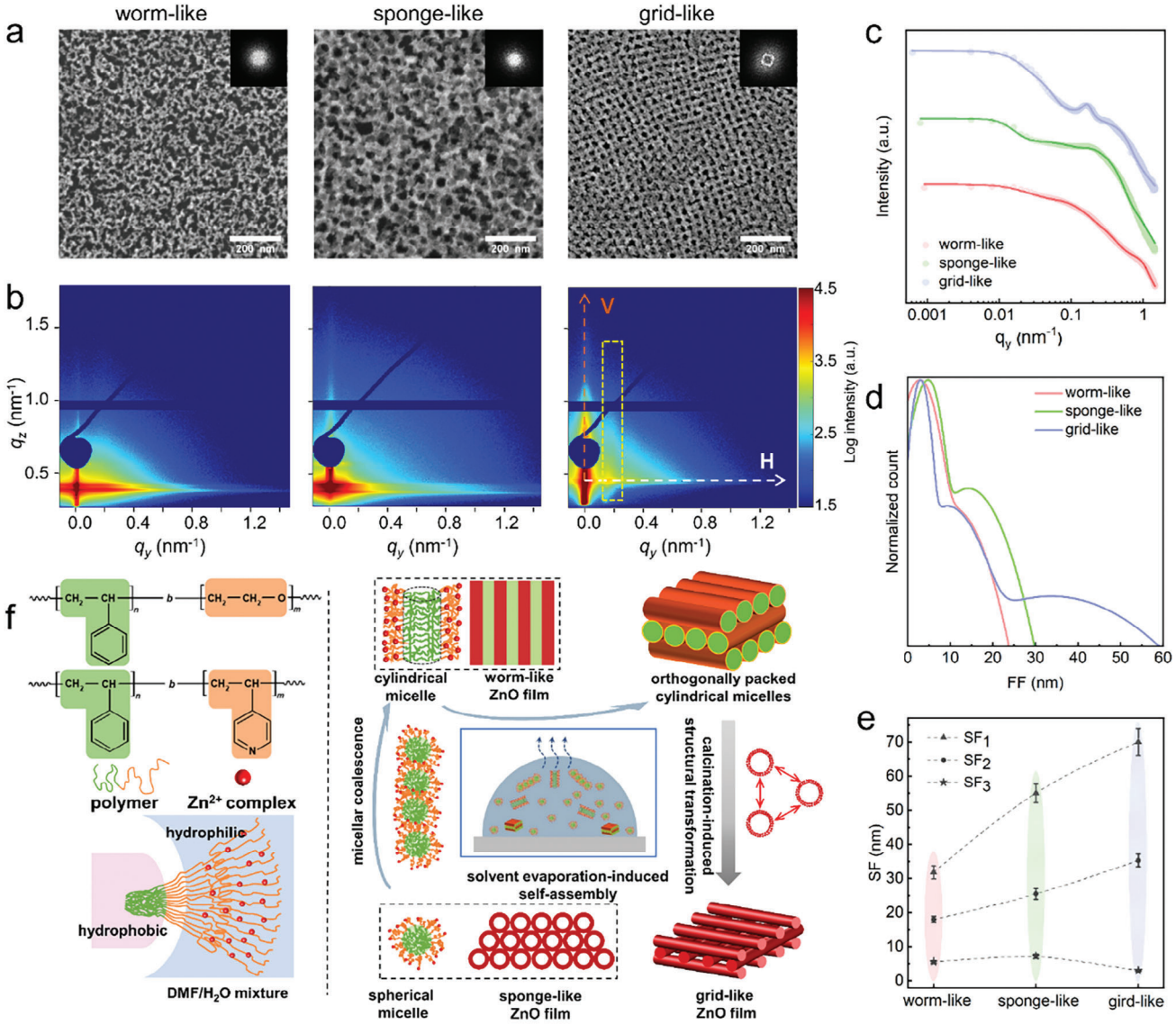

Figure 1. Surface and inner morphologies. a) Top-view SEM images and b) 2D GISAXS data of $PS_{20.5k}$-*b*-$PEO_{8.0k}$ templated worm-like (left panel), $PS_{20.5k}$-*b*-$PEO_{8.0k}$ templated sponge-like (middle panel) and $PS_{11.8k}$-*b*-$P4VP_{10.8k}$ templated grid-like (right panel) ZnO thin films. All samples share the same scale bar (200 nm). The orange and white dashed lines exemplarily display the directions for performing the vertical and horizontal line cuts, respectively, and the yellow rectangle highlights the peak positions of the characteristic Bragg reflection. c) Horizontal line cuts (filled circles) with respective modeling results (solid lines) of mesoporous ZnO films: worm-like, sponge-like, and grid-like from bottom to top. All curves are shifted along the vertical axis for clarification. d) Distribution functions of form factors (FF) and e) structure factors (SF) extracted from the fitting results. The triangles, circles, and blue stars denote the large-sized, middle-sized, and small-sized structures, respectively. The broken lines are guides to the eyes. f) The proposed formation mechanism of the mesoporous ZnO films based on the block copolymer self-assembly.

selected here due to the strong repulsive interaction between the hydrophobic PS and hydrophilic PEO (or P4VP) segments. The more detailed fabrication process can be found in the methods part of Figure S1 (Supporting Information). Scanning electron microscopy (SEM) images are first taken to reveal the surface morphologies of as-obtained mesoporous ZnO films after eliminating the sacrificial polymer templates via high-temperature calcination (**Figure 1**a). The completely different ZnO scaffolds are readily distinguished from the viewpoint of shapes, dimensions, and accessibility of pores. Irrespective of the polymer chosen as the building block, three representative samples exhibit pronounced structuring on the nanometer length scale, which predominantly benefits from the intrinsic self-assembly features of DBCs. The formation of a worm-like structured film (left panel in Figure 1a) is guided by the lower-molecular-weight $PS_{20.5k}$-*b*-$PEO_{8.0k}$ polymer, with the subscripts representing the number-average molar mass of the corresponding blocks. This porous film demonstrates randomly distributed yet highly interconnected ZnO nanostructures across the entire film volume. As opposed to this, the sponge-like film (middle panel in Figure 1a) templated by the higher-molecular-weight $PS_{60.0k}$-b-$PEO_{36.0k}$ polymer possesses relatively well-defined spherical pore

© 2023 The Authors. Advanced Functional Materials published by Wiley-VCH GmbH

arrays with more densely packed inorganic ZnO walls. In stark contrast, the grid-like film derived from the $PS_{11.8k}$-b-$P4VP_{10.8k}$ polymer exhibits more ordered structures, which highly resemble the nanowires stacked in an orthogonal way (right panel in Figure 1a). Such a discrepancy in structural ordering can also be reflected by the 2D Fast Fourier Transformation patterns shown in the insets in Figure 1a. Different from the fuzzy sphere characteristic of the former two films, the square-like feature observed in the grid-like film further verifies that the ZnO nanostructures are more regular in spatial arrangements. Correspondingly, the extracted power spectral density functions are shown in Figure S2 (Supporting Information). Compared to the others, a more well-defined peak shape in the grid-like ZnO film suggests its relatively higher level of nanostructural ordering, that is, such periodic arrangements are maintained over a larger macroscopic area. Meanwhile, the smallest inter-domain distance implies that the ZnO nanostructures in this film are more closely packed.

Grazing-incidence small-angle X-ray scattering (GISAXS) measurements are conducted to access the inner morphology changes of the mesoporous ZnO films, particularly to quantify the phase separation by determining the structural dimensions and spatial arrangements.[18] The selected incident angle (α_i) of 0.4° is higher than the critical angles (α_c) of the total external reflection of the films involved and of the substrate underneath, thus ensuring that the scattering signals are associated with the nanostructures of the entire mesoporous ZnO film. Figure 1b shows the corresponding 2D GISAXS data with distinct scattering intensity distributions along the in-plane and out-of-plane directions. In all cases, the films can be assumed as a two-phase system consisting of ZnO objects and empty pores with air inside. Thus, the detected scattering intensity is a function of their electron scattering density difference and volume fractions of them.[19] From the qualitative point of view, the distinct scattering contrasts reflect different packing modes of ZnO. As opposed to semicircular diffuse scattering features observed in the worm-like and sponge-like ZnO films, the vertically aligned Bragg rods are clearly visible in the grid-like ZnO film as marked by a dashed yellow rectangle in Figure 1b. This scattering phenomenon further confirms that the high degree of spatial arrangement is not only present on the film surface but propagates into the whole film thickness. As a macroscopic region of the films will be detected due to the large footprint of the X-ray beam, the scattering signals recorded are statistically relevant.[20] To gain quantitative insights into the as-obtained mesoporous ZnO films, vertical and horizontal intensity line cuts are performed, as exemplarily highlighted by dashed orange and white lines in Figure 1b, respectively.

The extracted vertical line cuts are plotted as a function of the exit angle (α_f), as shown in Figure S3 (Supporting Information). Beginning with the enhanced diffuse scattering given by the Fresnel transmission function, the local intensity maximum identified in the vertical cuts corresponds to the material-characteristic critical angle (α_c) and the so-called Yoneda region.[21] In the case of the grid-like ZnO film, multiple intensity modulations between the sample horizon and the specularly reflected beam position can be observed, which is caused by a dynamic scattering effect. However, the Yoneda peaks of these ZnO films can be easily distinguished to be morphology-dependent. According to the calculation of α_c from the scattering length density (SLD) at an X-ray wavelength (λ) of 1.54 Å, the constant peak at $\alpha_f = 0.206°$ in all mesoporous films can be assigned to the SiO_x/Si substrate. However, the α_c of mesoporous ZnO films is seen to shift from 0.135° to 0.157° to 0.223° when the morphology transforms from worm-like to sponge-like to grid-like. Considering that the chemical components of all involved mesoporous films are identical, the different α_c mainly arises from the presence of pores, that is, the different packing densities of the ZnO entities.

The scattering contrast in the GISAXS data is mainly proportional to the difference of the dielectric constants, which is often expressed by the complex refractive indices ($n = 1-\delta+i\beta$). With a negligible absorption term (β), n is mainly contributed by the dispersion (δ) term, which is closely relevant to the material category and corresponding physical density (ρ). α_c is associated with SLD according to[22]

$$q_c = \sqrt{16\pi \mathrm{SLD}} \tag{1}$$

where q_c denotes the α_c in reciprocal space. Based on wurtzite zinc oxide with a 1:1 molar ratio of Zn:O and density (ρ) of 5.61 g cm^{-3}, a theoretical nonporous SLD_n value of 4.27×10^{-5} $Å^{-2}$ can be determined. Accordingly, a direct comparison of SLD values of the mesoporous (SLD_m) and nonporous (SLD_n) ZnO materials allows a rough determination of the porosity (θ) of as-obtained ZnO thin films as follows:

$$\theta = 1-\frac{\mathrm{SLD_m}}{\mathrm{SLD_n}} \tag{2}$$

Therefore, the porosity can be estimated to be 32.7%, 25.4%, and 9.7% for the worm-like, sponge-like and grid-like ZnO films, respectively.

On the other hand, to quantify the differences in lateral morphology in more detail, the horizontal line cuts are integrated and plotted in Figure 1c. The shoulder-like feature occurring at different higher q_y positions for the worm-like and sponge-like ZnO film implies the absence of strong structural ordering, consistent with the morphological observation from SEM. In stark contrast, a prominent peak emerges in the grid-like ZnO film located in between, which can be attributed to the significantly improved spatial correlations of the ZnO domains. To provide in-depth insights into the mesoporous ZnO films, these cuts are further modeled using the framework of the distorted wave Born approximation (DWBA) and effective interface approximation (EIA).[23] On the basis of the SEM images, a cylindrical geometry appears most suitable and thus is applied to model the ZnO domains for all mesoporous films. As the ZnO domains are assumed to be locally distributed in a 1D paracrystalline lattice with a Gaussian distribution, the form factors (FFs) and structure factors (SFs) of ZnO domains can be resolved from the modeling results, in which FF and SF define the domain radius and inter-domain distance, respectively. Three sets of characteristic structures are applied for successful modeling for all cases and the detailed structural parameters are extracted. The subscripts 1, 2, and 3 used in the FF and SF denote the large-sized, medium-sized, and small-sized ZnO domains, respectively. Taking worm-like ZnO film as an instance, FF_1, FF_2, and FF_3 are (10.4 ± 0.9) nm, (4.4 ± 0.5) nm, and (2.0 ± 0.4) nm, respectively (Figure S4a, Supporting Information), and the corresponding SF_1, SF_2, and SF_3 are (31.8 ± 1.9)

© 2023 The Authors. Advanced Functional Materials published by Wiley-VCH GmbH

nm, (18.0 ± 0.9) nm, and (5.5 ± 0.3) nm, respectively (Figure 1e). According to the corresponding domain size distribution plotted in Figure 1d, the quantity and volume fraction can be calculated (Figure S4b,c, Supporting Information).[24] With the highest number and volume fraction, the FF_1 constitutes the majority contribution of this film. The sponge-like ZnO film shows marginally enlarged FFs and SFs, with FF_2 accounting for the highest volume fraction. As magnified by a narrower arc in the distribution function, the presence of FF_3 is more pronounced in the grid-like ZnO film, but FF_1 plays a dominant role in both the amounts and the volume. Simultaneously, the SF_1 is even smaller than the other two cases, which might also facilitate the ions transport via the hopping mechanism.

The structural differences observed here are mainly derived from the self-assembly of the BCP, in which the PS serves as the pore-forming agent, and Zn-rich PEO or P4VP phases define the organic-inorganic hybrid matrix and final skeletal ZnO networks. Specifically, the formation of mesoporous ZnO films through a BCP-based wet chemical approach highly depends on the synergistic and competitive interplay between BCP physics and sol–gel chemistry. In a precursor-incorporated hybrid system, phase separation begins with composite micelles/aggregates in the solution state, as defined by the intermolecular interactions and the packing parameters. Initiated by the N, N-dimethylformamide (DMF)/water (H_2O) co-solvent, the intrinsic incompatibility between the covalently connected two phases of BCP gives rise to assembled BCP micelles due to a natural tendency for interfacial energy minimization. Despite being chemically distinct, PEO and P4VP have similar solubility parameters and interactions with the used solvent. Thus, a possible effect originating from the BCP type is minor.[25] Meanwhile, the commercially available ZnO precursors get hydrolyzed, resulting in complex intermediate products abundant with hydroxyl (OH) functional groups.[26] Upon mixing, these polar OH groups prefer to interact with polar ether groups on the PEO blocks or the pyridine groups on the P4VP blocks through intermolecular hydrogen bonding, thus rendering the inorganic components an integral part of the organic polymer.[27] Alternatively, the electron-deficient Zn can also directly accept the lone-pair electron from the oxygen atom on PEO or the nitrogen atom on P4VP through the metal coordination effect.[28] As such, the inorganic phase will be molecularly tethered to the polymer chains and selectively located in these PEO/P4VP-rich domains. Although relatively stronger electrostatic interactions can significantly change the phase separation behavior, their possible presence can be excluded by considering the fact that i) no additional acids or bases are added and ii) the zinc salt used as a precursor has a low solubility and dissociation constant.[29] According to the morphological observations, the possible formation mechanisms of the mesoporous ZnO films are speculated, as schematically illustrated in Figure 1f. In the case of sponge-like film, it is easy to identify the round dark area embedded within the white framework, which hints that the spherical composite micelles are kinetically frozen during processing. In appearance, the worm-like ZnO film shares some similarities with the flexible cylindrical micelles, which might be generated directly or transformed from spherical ones due to solvent evaporation-induced self-assembly. Analogous to the previous report, the grid-like ZnO film is made possible through orthogonally packed cylindrical micelles to minimize the repulsive interactions between neighboring stacking layers.[30] During the subsequent calcination process, polymer decomposition, sol–gel condensation, and ZnO crystallization would occur simultaneously and induce further transformation into grid-like nanostructures.

2.2. Structural Characteristics

Having identified the role of the self-assembly strategy in guiding the morphology on the nanometer length scale, next the crystalline behavior of the inorganic ZnO frameworks at a smaller spatial level is explored. **Figure 2**a displays the 2D grazing incidence wide-angle X-ray scattering (GIWAXS) data of as-obtained mesoporous ZnO thin films after geometrical corrections. The dark wedge-shaped regions indicate the partially missing scattering signal along the out-of-plane direction due to the curvature of the Ewald sphere.[31] Despite the abundant presence of pores in all films, only the ZnO frameworks have a GIWAXS scattering contribution. Theoretically, sharp diffraction intensity in the GIWAXS data would be expected for a highly crystalline ZnO sample. However, only a much broader scattering ring ranging from 1.9 to 2.8 $Å^{-1}$ is distinguishable for all mesoporous ZnO films, evidencing a suppressed crystallization behavior due to the presence of pores and nanostructures. This behavior is particularly the case for the metal oxides synthesized with surfactants or amphiphilic DBCs as structure-directing agents. Generally, during such a cooperative assembly of organic and inorganic components, there would be a competitive interplay between the crystallization degree of inorganic species and phase-separated behaviors generated by the organic template. Although some strategies to prevent template collapse and improve the cross-linking of the inorganic precursors have been developed, achieving well-defined mesostructures and highly crystalline frameworks simultaneously yet independently has been challenging.[32] Despite this, we can find that the grid-like ZnO thin film has relatively stronger and sharper diffraction signals compared to the other two, which can be qualitatively interpreted as improved crystallinity. To probe the origins of such a diffraction feature in more detail, 1D scattering profiles are extracted from 2D GIWAXS data by azimuthal integration performed from −50° to 88° in χ direction (so-called radial cake cuts), as plotted by circles in Figure 2b. Notably, these line cuts extracted from GIWAXS data can provide information comparable to the conventional X-ray powder diffraction (XRD), thus allowing the identification of the phase of formed ZnO crystals. For all cases, three characteristic scattering peaks can be distinguished with the most pronounced one located at a medium momentum transfer q of ca. 2.4 $Å^{-1}$. Additionally, two weaker shoulders positioned at lower q of ca. 2.2 $Å^{-1}$ and higher q of ca. 2.6 $Å^{-1}$ are also present. By transforming the q space into diffraction angles (2θ) ($q = \frac{4\pi}{\lambda}\sin(2\theta/2)$, where λ is the wavelength of the X-ray), these peaks are characteristic of the hexagonal wurtzite ZnO phase with a $P6_3mc$ symmetry (JCPDS, card No 36–1451).[33] Compared to the other polymorphs of ZnO, the wurtzite structure is more thermodynamic stable. Accordingly, the scattering peaks from the low q to high q region can be indexed to (100), (002), and (101) Bragg reflections, respectively. Nevertheless, some differences in crystalline behavior are present and can be investigated in

© 2023 The Authors. Advanced Functional Materials published by Wiley-VCH GmbH

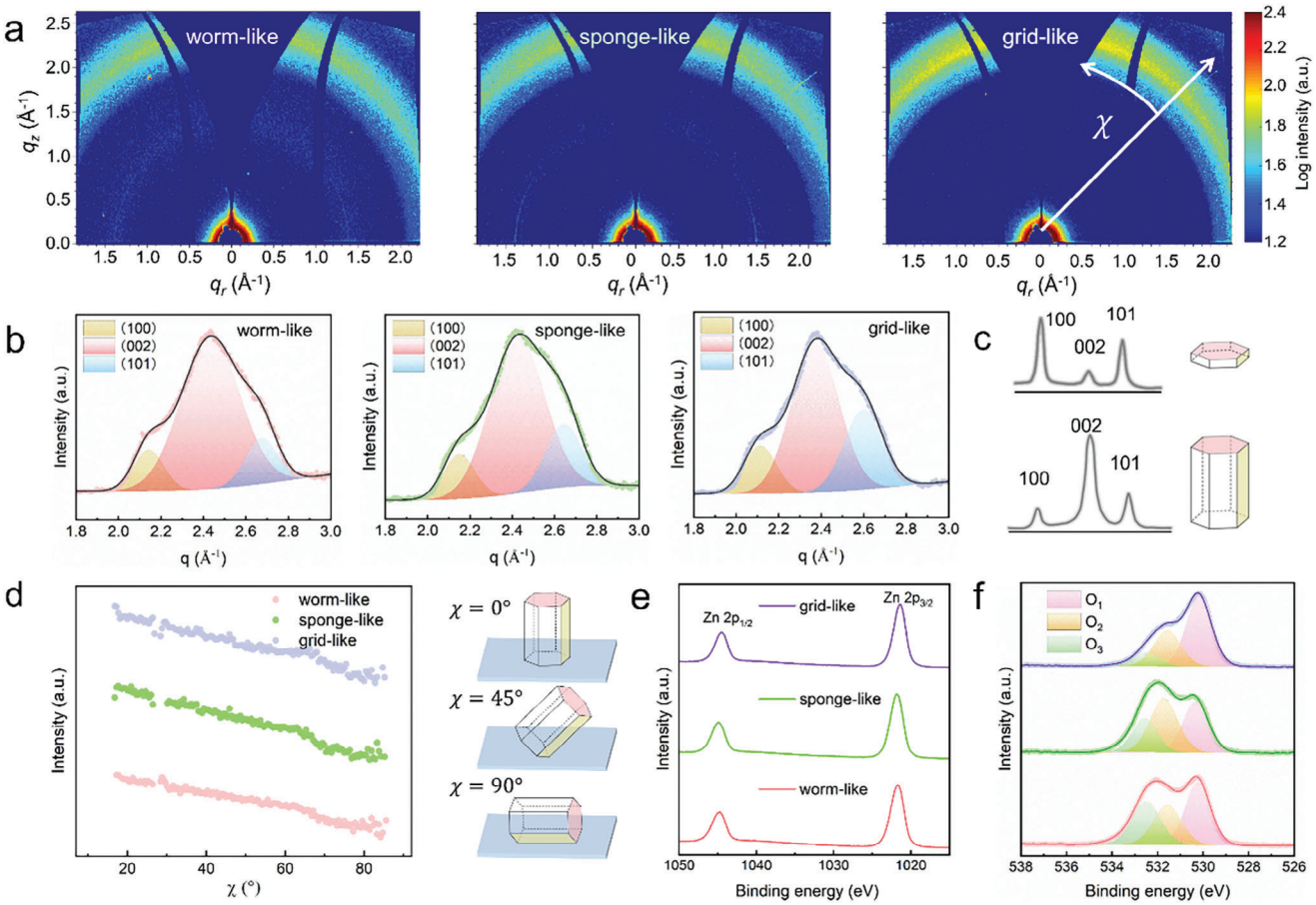

Figure 2. Crystallinity and orientation analysis. a) Reshaped 2D GIWAXS data of worm-like (left panel), sponge-like (middle panel), and grid-like (right panel) mesoporous ZnO films. b) 1D radial cake cuts obtained from the 2D GIWAXS data of worm-like (left panel), sponge-like (middle panel), and grid-like (right panel) mesoporous ZnO thin films, providing *pseudo*-XRD information. Original cuts and the fit results are represented by circles and solid lines, respectively. c) Diagram illustrating hexagonal ZnO crystals with different aspect ratios (upper row) and resulting intensity ratios in GIWAXS data (bottom row). d) Pole figures of the predominant (002) peak showing the intensity of (002) reflection as a function of azimuth angle χ, all curves are normalized. The associated hexagonal ZnO crystal orientations aligned at different χ values are also shown. High-resolution XPS spectra of e) Zn 2p and f) O 1s for mesoporous ZnO films.

a quantitative manner. Therefore, the position, amplitude, and full width at half maximum (FWHM) of the peaks are further extracted through curve fits with a Gaussian profile, as summarized in Table S1 (Supporting Information). It is worth noting that the peak center q for each crystal plane remains almost constant irrespective of the morphological differences between these films, thus revealing a nearly negligible change in the corresponding interplanar spacing d_{hkl}. It was well-documented that the relative amplitude of (100) and (002) planes in the XRD data can be used as a shape factor to reflect the anisotropy degree of hexagonal ZnO crystals. In general, the scattering intensity of one specific plane in the crystal structures is directly proportional to its quantity and reflects the distribution of constituting atoms along the crystallographic axis. For bulk, a ratio of 1.17 for (100)/(002) is typical of isotropic ZnO particles, so shape changes would be manifested as deviations from this value.[34] An increased (100)/(002) ratio represents the presence of short cylinders or even more flattish disks. Conversely, a substantially diminished (100)/(002) ratio is closely associated with the formation of more elongated rods, as illustrated in Figure 2c. Such shape change has been commonly observed in the additives-engineered synthesis of hexagonal ZnO crystal, predominantly due to the different growth kinetics of crystal planes mediated by the selective adsorption of additives onto the specific ZnO surface.[35] As the (002) peak shows a maximum amplitude in the GIWAXS data for all films, ZnO crystal structures can be differentiated to be more rod-like with preferential growth along the c-axis direction. In this scenario, six relatively longer nonpolar prismatic faces (lateral surfaces highlighted by yellow in Figure 2c) are capped by two polar basal planes (top surfaces highlighted by pink in Figure 2c). With a hexagonal structure and preferential growth along the c-axis direction retained in all mesoporous ZnO films, the BCP-templated synthesis does not alter the crystal type nor impede the crystal growth along a specific plane.

The (002) reflection is chosen as a yardstick for further comparison as it is the most intense in scattering data. Interestingly, the FWHM of the (002) peak follows a decreasing tendency from worm-like (0.327 Å^{-1}) to sponge-like (0.303 Å^{-1}) to grid-like (0.264 Å^{-1}) ZnO film, implying the gradually improved crystallinity. Correspondingly, the crystallite size D_{002} is determined

© 2023 The Authors. Advanced Functional Materials published by Wiley-VCH GmbH

based on the Scherrer formula, and an inversely increasing trend can be given for worm-like (1.79 nm) to sponge-like (1.93 nm) to grid-like (2.21 nm) ZnO film. Moreover, we use the integrated intensity of the most intense (002) peak to evaluate the structural perfectness by calculating the relative degree of crystallinity (RC), which can be deduced from the azimuthal integration of the (002) Bragg reflection against the polar angle χ by using[36]:

$$\mathrm{RC} \propto \int_0^{\frac{\pi}{2}} \mathrm{I}(\chi)\sin\chi \mathrm{d}\chi \tag{3}$$

where χ is defined as the angle between the scattering vector q with respect to the q_z axis, as illustrated in the inset of the 2D GIWAXS data (Figure 2a), and sin χ is applied for a baseline correction to account for the isotropic population. The values $\chi = 0°$ and $\chi = 90°$ denote the out-of-plane (q_z) and in-plane (q_r) direction, respectively. More detailed crystallographic parameters can be found in Table S2 (Supporting Information). With the RC value of grid-like ZnO film being normalized to 1, the worm-like and sponge-like ones exhibit a decreased RC of 0.64 and 0.72, respectively, implying that the morphology plays a role in affecting the crystallization behaviors to some degree. From the perspective of the crystallization process, the suppressed ZnO crystallization in mesoporous films is speculated to be a result of sterically hindered nucleation and growth due to the abundant presence of empty pores or polymer chains. Thus, the relatively improved crystallinity in the grid-like film could be ascribed to the smaller pore dimensions compared to the others. With a Bragg-Brentano geometry and a 1D detector, the q-range that can be probed by XRD is mainly concentrated at $q_r = \sqrt{q_x^2+q_y^2} = 0$. In contrast, a larger q_r detection range can be obtained in GIWAXS, so that structural information regarding the crystal planes that are not perpendicularly oriented can be resolved.[37] As for crystallites with high orientation degrees, discrete diffraction spots at specific q values or diffraction arcs along different azimuthal angles can be identified in GIWAXS data. On the contrary, the pronounced angular spreading of the (002) plane with higher scattering intensity along the out-of-plane direction appears in all mesoporous ZnO films, confirming that a large portion of the crystallites is randomly distributed despite a slight orientational preference. This finding can be further corroborated by the pole figures of (002) reflection exhibited in Figure 2d. Irrespective of the morphological difference, all mesoporous ZnO films demonstrate the highest scattering intensity near the $\chi = 0°$, characteristic of a preferential face-on packing of the (002) plane. In the field of organic and perovskite photovoltaics, the preferentially oriented crystals play a significant role in determining the corresponding device performance.[38] Analogously, such a slightly preferred orientation is also speculated to facilitate the charge carrier transport in ZnO films. Moreover, these decay curves are almost parallel without any discernible slope differences in the entire χ range, indicating negligible variations in orientation distribution among these films. Notably, this behavior can be differentiated from the isotropic orientation featuring a complete averaging of the unit cell orientation, which involves homogeneously distributed scattering intensity. Although the selected polymers play an essential role in dictating the spatial arrangements of the ZnO frameworks on the nanoscale, the polymorph type, growth preference, and texture of resultant ZnO crystals remain substantially unaltered.

The high level of porosity but weak crystalline feature indicates that the as-obtained ZnO structures could be abundant in some intrinsic defects. Therefore, X-ray photoelectron spectroscopy (XPS) analysis is carried out to give insights into the defect chemistry on the mesoporous film surface. Irrespective of film morphology, all samples show one doublet in the core-level Zn 2p spectra corresponding to Zn $2p_{3/2}$ and Zn $2p_{1/2}$ electron states with binding energies (BE) of 1021 and 1045 eV, respectively (Figure 2e), evidencing the "2^+" valence state of Zn ions.[39] Figure 2f illustrates the corresponding O 1s spectra, which reveal BE deconvoluted into three different sub-peaks at ≈ 530.2 eV (O_1), ≈ 531.6 eV (O_2), and ≈ 532.7 eV (O_3). The O_1 and O_3 can be unambiguously attributed to the O^{2-} ions in the ZnO lattice and irreversibly adsorbed water molecules, respectively. However, the interpretation of the O_2 signal has been controversial. Although a lot of existing works attribute it to oxygen vacancies (O_v) to account for their dominant role in surface chemistry and property of metal oxides,[40] some reports point out that surface hydroxyl groups (OH) are the more plausible explanations due to dissociatively adsorbed water molecules.[41] From the perspective of the XPS mechanism, missing oxygen atoms are beyond the detection range of XPS and unavoidable moisture exposure of samples in ambient environments before transferring into the measurement chamber, ex situ measurements of surface O_v are not possible.[42] Nevertheless, extensive studies have established that O_v can act as active sites and participate in the defect-chemical reactions, facilitating the chemical dissociation of water and subsequent generation of OH. Therefore, the more precise interpretation of the O_2 peak here is the surface OH, which can serve as indirect evidence about the presence of O_v in all mesoporous ZnO films. Analogous to other metal oxides, the generation of O_v most possibly originates from the high-temperature annealing process.[43]

Following this, photoluminescence (PL) and ultraviolet-visible (UV–vis) spectroscopy were conducted to gain insights into the optoelectronic properties of the obtained mesoporous ZnO film. As illustrated in Figure S5a (Supporting Information), the most intense absorption in the UV–vis spectra is located at the UV region for all mesoporous ZnO films. By using Tauc's plot, the corresponding bandgap energy (E_g) is estimated to be 3.20 eV for sponge-like, 3.15 eV for worm-like, and 3.12 eV for grid-like ZnO film (Figure S5b, Supporting Information). Typical of an n-type semiconductor with a wide bandgap, the E_g of wurtzite ZnO bulk is usually reported to be in the range of 3.1–3.4 eV.[44] In good consistency with this, the largely unaltered E_g values further verify that the intrinsic optical properties of wurtzite ZnO are well retained in all mesoporous ZnO films. Moreover, an appreciable tail in the visible range of the UV–vis spectra can be identified, accompanied by slightly enhanced absorbance from sponge-like to worm-like and then to grid-like (Figure S5a, Supporting Information). Similar sub-band optical absorption has been documented in ZnO and other semiconductors with underlying origin assigned to the existence of defects.[45] In this scenario, such an absorption feature is closely associated with O_v, as suggested by the above XPS and following PL results. By contrast, such absorption is indistinguishable in the case of wurtzite ZnO without O_v.[46] Therefore, the contents of O_v increase from

© 2023 The Authors. Advanced Functional Materials published by Wiley-VCH GmbH

sponge-like to worm-like and then to grid-like ZnO film as indicated by their relative intensity. As displayed in the complementary PL spectra (Figure S6, Supporting Information), the band-to-band recombination-induced near-band edge (NBE) emissions in the UV region appear in all mesoporous films, as expected for wurtzite ZnO structures. Concomitantly, broad green emissions can be found. This is correlated with the radiative recombination between the photo-induced hole and the electron occupying the O_v.[47] The relative intensity ratio of green and UV emission has been commonly used as a benchmark to quantify the O_v levels. Correspondingly, the defect levels in mesoporous ZnO films follow a sequence of grid-like> worm-like> sponge-like, in good consistency with the UV–vis results.

2.3. Water Adsorption on ZnO Surfaces

The experimental findings mentioned above strongly indicate the presence of abundant O_v within the mesoporous ZnO films. From an atomic level, density functional theory (DFT) calculations are used next to investigate the effect of O_v on water adsorption and the electronic structure of ZnO surfaces. Typical of a hexagonal wurtzite crystal cell, ZnO exhibits three possible surfaces with nonpolar $(10\bar{1}0)$ surfaces representing the sides of the hexagon, polar Zn-terminated (0001) and O-terminated $(000\bar{1})$ surface at the top and bottom of the hexagon, respectively. As dominant surfaces for ZnO powder and single crystals, nonpolar $(10\bar{1}0)$ facets containing equal numbers of Zn and O atoms are more stable and have been the most investigated, both theoretically and experimentally. As (002) reflection prevails in the GIWAXS data of all mesoporous ZnO films in this work, the polar (0001) surfaces are selected for further calculations. We use a six-layer slab model containing 48 Zn and 48 O atoms, with the bottom two layers of atoms being fixed and a vacuum region of 15 Å at the surface. The strong correlation between Zn 3d electrons in the lattice is accurately described by introducing a localized coulomb repulsion U term in the calculations, known as the GGA+U method.[48] More details about the calculation methods can be found in Figures S7 and S8 (Supporting Information). The surface configuration plays an important role in determining water adsorption by creating different chemical environments. Figure S8a,b (Supporting Information) illustrates the ZnO (0001) surface structures with two different types of coordinations (tri-coordinated and mono-coordinated) and terminations (Zn and O), and the corresponding surface energy can be evaluated as follows:

$$E_{\mathrm{surf}}^{\mathrm{i_j}} = E_{\mathrm{Relax}}^{\mathrm{i_j}} + E_{\mathrm{c}}^{\mathrm{j}} \tag{4}$$

where $E_{\mathrm{surf}}^{\mathrm{i_j}}$ is the surface energy per unit area of the surface with j-coordination and i-atom termination, $E_{\mathrm{Relax}}^{\mathrm{i_j}}$ is the relaxed energy per unit area of i_j surface, and $E_{\mathrm{c}}^{\mathrm{j}}$ is the cleavage energy per unit area of the surface with j-coordination. The $E_{\mathrm{surf}}^{\mathrm{i_j}}$, $E_{\mathrm{Relax}}^{\mathrm{i_j}}$ and $E_{\mathrm{c}}^{\mathrm{j}}$ of the tri-coordinated O (O_t), tri-coordinated Zn (Zn_t), mono-coordinated O (O_m) and mono-coordinated Zn (Zn_m) surfaces are summarized in Table S3 (Supporting Information). Compared to the O_m and Zn_m surfaces, the lower $E_{\mathrm{c}}^{\mathrm{j}}$ of the O_t and Zn_t surfaces predicts the higher possibility of broken bonds between the atoms. Similarly, the $E_{\mathrm{Relax}}^{\mathrm{i_j}}$ of the O_t and Zn_t surfaces is also found to be lower than the O_m and Zn_m surfaces, indicating that the O_t and Zn_t surfaces are more inclined to undergo a surface reconstruction. As a consequence, the significantly lower $E_{\mathrm{surf}}^{\mathrm{i_j}}$ of O_t (1.01 J m^{-2} for O_t vs 5.44 J m^{-2} for O_m) and Zn_t (0.83 J m^{-2} for Zn_t versus 5.59 J m^{-2} for Zn_m) surfaces implies they are more energetically favorable for water adsorption and are considered for subsequent calculation.

For both cases of O_t and Zn_t, there is only one type of O_v site. Figure S8c (Supporting Information) displays the geometrical configurations of O_t and Zn_t surfaces with O_v formation sites and water adsorption sites. By comparing the formation energy of O_v ($E_{v,\mathrm{form}}^{\mathrm{i_j}}$) on different ZnO (0001) surfaces (Table S3, Supporting Information), we can find that the $E_{\mathrm{v,form}}^{\mathrm{i_j}}$ of the ZnO supercell is comparable to that of the Zn_t surface. Distinguishably, the O_t surface prefers the generation of O_v, as suggested by the lowest $E_{\mathrm{v,form}}^{\mathrm{i_j}}$ of 1.18 eV. Considering this, the water adsorption behavior is first investigated on the O_t surface, and the corresponding atomic and electronic structures after water adsorption are illustrated in **Figure 3**. The corresponding adsorption energies (E_{ad}) of water molecules on different O_t or Zn_t surfaces with and without O_v are listed in Table S4 (Supporting Information). According to the optimized structural configurations, there are two possible adsorption sites on the O_t surface before the O_v generation: Zn and O. The water molecules adsorbed to other sites are found to be migrated to these two sites (represented as To O and To Zn as shown in Table S4, Supporting Information). As is typically the case for water adsorption, a hydrogen bond (H bond) tends to form between the H atom of the water molecule and the O atom on the ZnO surface. On the other hand, a Zn—Ow bond would occur between the O atom from the water molecule (Ow) and the Zn atom on the ZnO surface. At the Zn site (Figure 3a), the water molecule is adsorbed to the surface in a parallel configuration with an E_{ad} of −0.22 eV. At the O site (Figure 3b), the H atom of the water molecule is perpendicularly attached to the exposed O atom via a H bond with an E_{ad} of −0.12 eV. In the existence of O_v (Figure 3c), the water molecule is mainly adsorbed onto the Bridge site that connects the Zn atom and neighboring O atom (as detailed in Figure S8c, Supporting Information). As shown in the side views (middle columns in Figure 3a–c), O_v also facilitates the emergence of a different Zn—O_w bond. Despite this, the corresponding bond length demonstrates an almost negligible variance upon molecular binding of water to the ZnO surface (2.19 vs 2.18 Å). Meanwhile, a newly formed H bond with a bond length of 1.79 Å can be identified, as highlighted by a purple line in the middle panel of Figure 3c. Compared to the Zn and O sites, the E_{ad} of the Bridge site reduces to −0.80 eV (Table S4, Supporting Information), implying that the chemical adsorption of water is more thermodynamically favorable on an O_t surface due to the O_v formation. In the absence of O_v, no substantial differences in the charge density of the Zn—Ow or H bond can be observed (right panels in Figure 3a,b). However, accumulation and depletion regions of charge density appear simultaneously for both Zn—O_w and H bond upon O_v formation (right panel in Figure 3c). In good consistency with the E_{ad} results, these observations further evidence the critical role of O_v on the Zn_t surfaces.

© 2023 The Authors. Advanced Functional Materials published by Wiley-VCH GmbH

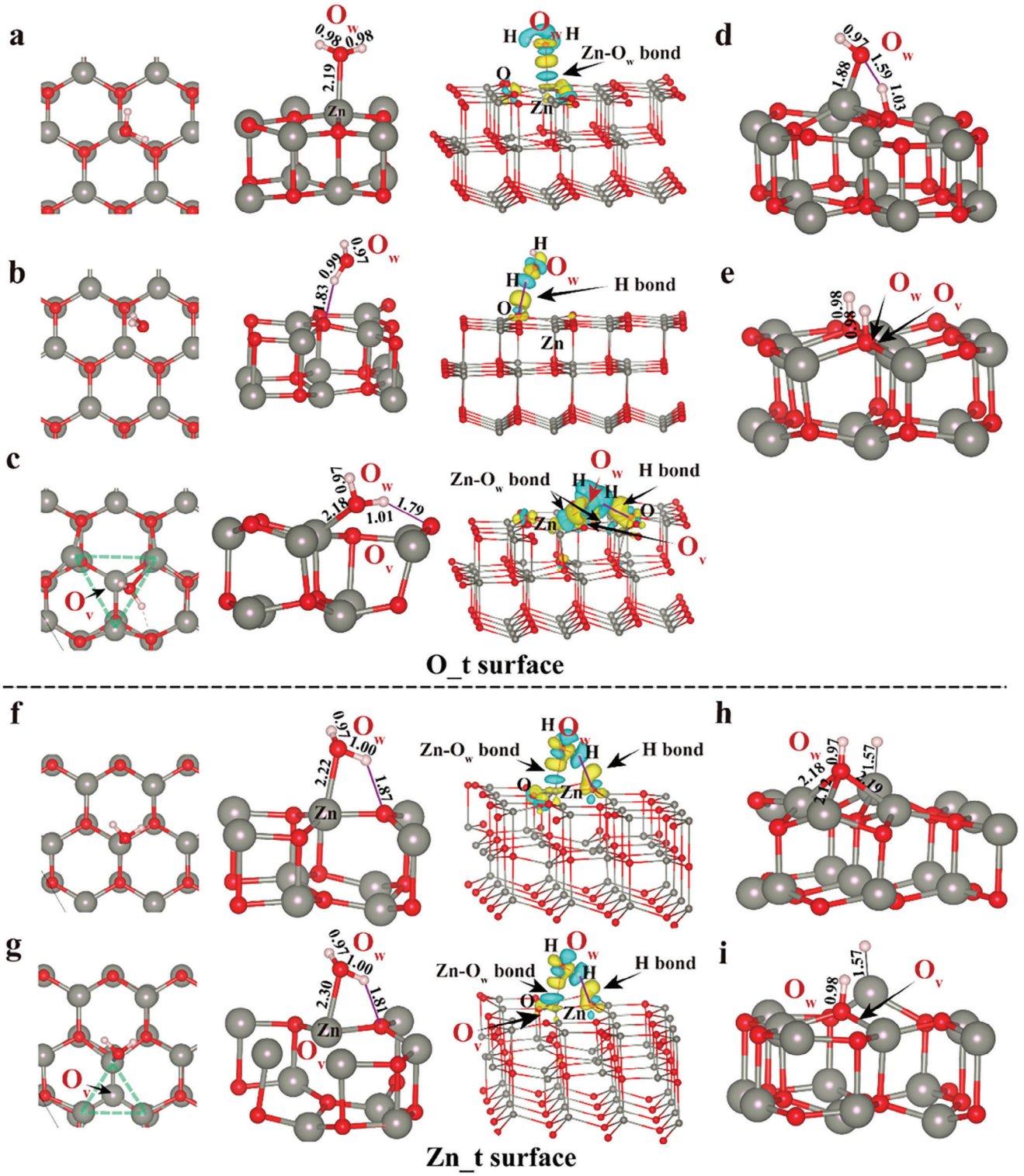

Figure 3. Representations of the O_t surface with the water molecule adsorbed at a) Zn site without O_v, b) O site without O_v, and at c) Bridge_v position with O_v, and of the Zn_t surface with the water molecule adsorbed at Zn site f) with and g) without O_v. The left, middle, and right columns are the top views, side views with marked bond lengths, and corresponding charge density difference maps, respectively. The side views of the most stable structure when adsorbed H_2O molecule was dissociated at Zn site on O_t surface d) without and e) with O_v, and on Zn_t surface h) without and i) with O_v. Zn, O, and H atoms are depicted in gray, red, and pink, respectively. O_v denotes the oxygen vacancy in the ZnO lattice, and O_w is the oxygen atom from the water molecule, respectively. Zn—O_w bond represents the interaction between Zn atom and O_W, and H bond is the hydrogen bond. The yellow and cyan regions represent the increase and decrease of charge in this region, respectively. The iso-value for the plot is taken as 0.002 e bohr^{-3}.

© 2023 The Authors. Advanced Functional Materials published by Wiley-VCH GmbH

Next, the water adsorption on the Zn_t surface is also explored (Figure 3f,g). Analogously, only the Zn site is discussed as the water molecules adsorbed to other sites are found to migrate to this site. Compared to the O_t surface, it is more difficult for the Zn_t surface to generate O_v, as manifested by a higher $E^{i_j}_{v,form}$ of 3.90 eV. However, the H bond length decreases from 1.87 to 1.81 Å, indicative of a stronger interaction between ZnO surface and water molecule upon O_v generation. While the Zn—O_w bond is weakened, as reflected by an increased Zn—O_w bond length from 2.22 to 2.30 Å (middle panels in Figure 3f,g). However, the E_{ad} of water on the Zn site shows slight variation before (−1.45 eV) and after (−1.31 eV) the generation of O_v (Table S4, Supporting Information). The negative values here are typical for an exothermic process, indicating that water molecules can be spontaneously adsorbed on the Zn_t surface irrespective of the occurrence of the O_v. Therefore, the impact of O_v is almost negligible in water molecule adsorption on the Zn_t surface. To further elucidate the role of O_v on the adsorption and dissociation of water molecules, the structures of the water molecule at the most stable adsorption sites before and after the generation of O_v on Zn_t and O_t surface are calculated, as shown in Figure 3d,e,h,i. The corresponding dissociation energy (E_{dis}) results are summarized in Table S4 (Supporting Information). As accompanied by the adsorption and subsequent dissociation of a water molecule, the generation of an OH group and a H atom is expected. Without O_v, the dissociated OH group is located at the Zn and hollow sites for O_t and Zn_t surfaces, respectively (Figure 3d,h). However, the presence of O_v facilitates the migration of oxygen atom in the OH group to the O_v site for both cases (Figure 3e,i), leading to a significantly reduced E_{dis} of water molecules. Compared to the decreased E_{dis} from 0.12 to −0.50 eV upon the generation of O_v for the Zn_t surface, this effect is more evident for the O_t surface as reflected by more significantly reduced E_{dis} from 0.19 to −1.48 eV.

Taken together, the adsorption and subsequent dissociation of water molecules on the ZnO surfaces are complex processes and highly dependent on the types of termination and coordination. Besides, O_v can act as an active site, giving rise to a beneficial effect for water adsorption on the ZnO film surface, followed by chemical dissociation contributing to the ionic conductivity as discussed below. These calculation results are also consistent with the theoretical investigations on the rutile TiO_2 surfaces.[49]

2.4. In Situ Investigations

The morphology would affect the water adsorption from multidimensions, consequently regulating the electrical properties of mesoporous ZnO films. The water contact angles of all mesoporous ZnO films are in the range of 24°–34°, indicating their rather hydrophilic nature (Figure S9, Supporting Information). As reported previously, there is no linear correlation between structural characteristics and electrical properties of mesoporous ZnO film, as multiple factors would govern the water adsorption process.[50] Generally speaking, the high porosity and large pore size are mainly responsible for providing effective pathways for water vapor diffusion into the ZnO layer, thus providing more possibility for water adsorption. The presence of O_v also plays an essential role in water adsorption and dissociation, and a higher level of O_v is expected to give rise to a higher water adsorption capability. Besides, the dominant morphological factor for humidity sensing at low RH is specific surface area, while the mesopore volume is important for high RH, as capillary condensation would occur at this condition. Given such synergistic effects, a more detailed analysis is challenging for limited samples in the present work. However, we aim to capture a general framework for the structure-property relationship of the BCP-derived mesoporous films during water adsorption.

Figure 4a presents the schematic in situ setup used to gain more in-depth insights into the correlations between water adsorption, electrical properties, and morphology evolution of different mesoporous ZnO films by means of combined Fourier-transform infrared (FTIR), alternating current (AC) impedance spectroscopy and GISAXS measurements. The films are mounted inside a homemade chamber connected to a vapor generation system providing an adjustable humidified gas flow. By progressively increasing the ratio between dry nitrogen (N_2) and saturated water (H_2O or D_2O) vapor from 0% to 100%, the relative humidity (RH) level of the sample environment is controlled. For instance, the measured humidity is 2–7% RH and 78–82% RH when the set-point of water vapor is 0% and 100%, respectively. More details about the measured RH values can be found in Table S5 (Supporting Information). In the following, we use the setting values of water vapor to describe the RH changes unless otherwise pointed out.

As schematically illustrated in Figure 4b, both chemisorbed and physisorbed water species can be present on the ZnO surfaces depending on the humidity levels. Starting from the molecular-level interactions, in situ FTIR measurements are performed to provide traceable clues about RH-dependent water chemistry on the ZnO film surface. Considering that all mesoporous ZnO films are covered by surface hydroxylates or water species revealed by the XPS results above, a D_2O atmosphere is exclusively used for RH control of the FTIR part. Possible DMF residuals can also interact with water molecules and interfere with the defect-related water adsorption process due to the formation of a hydrogen bonding network. However, such an effect can be excluded in the present study by the high-temperature annealing process (400 °C), as supported by the absence of DMF-related characteristic vibration signals in the FTIR spectra.[51] In the FTIR spectrum, the water-related (H_2O or D_2O) signals would appear in the form of broad absorption bands, which are a superposition of several sub-bands characteristic of different vibrations of free and hydrogen-bonded water molecules.[52] After drying to the minimum RH (set-point 0% H_2O, i.e., measured humidity 2–7% RH), a broad H_2O absorption band centered at 3440 cm^{-1} is clearly visible in the FTIR spectra of all samples (Figure S10, Supporting Information). Such a non-negligible presence of water on the ZnO surface is most possibly from the chemical adsorption, which is once formed and cannot be further eliminated by a simple drying procedure. In addition, the stronger and sharper peaks observed at 1577 and 1385 cm^{-1} are associated with asymmetric and symmetric stretching modes of the carboxylate group (COO—) from acetate species, signifying the existence of ZnO precursor residuals on the film surface.[53] Such significant traces of residual carbon in ZnO are typical of solution-based synthesis, especially with an applied temperature gradient of less than or equal to 400 °C. As elucidated by the in situ FTIR spectra displayed in Figure 4c, a single trend as a function of RH level can be

© 2023 The Authors. Advanced Functional Materials published by Wiley-VCH GmbH

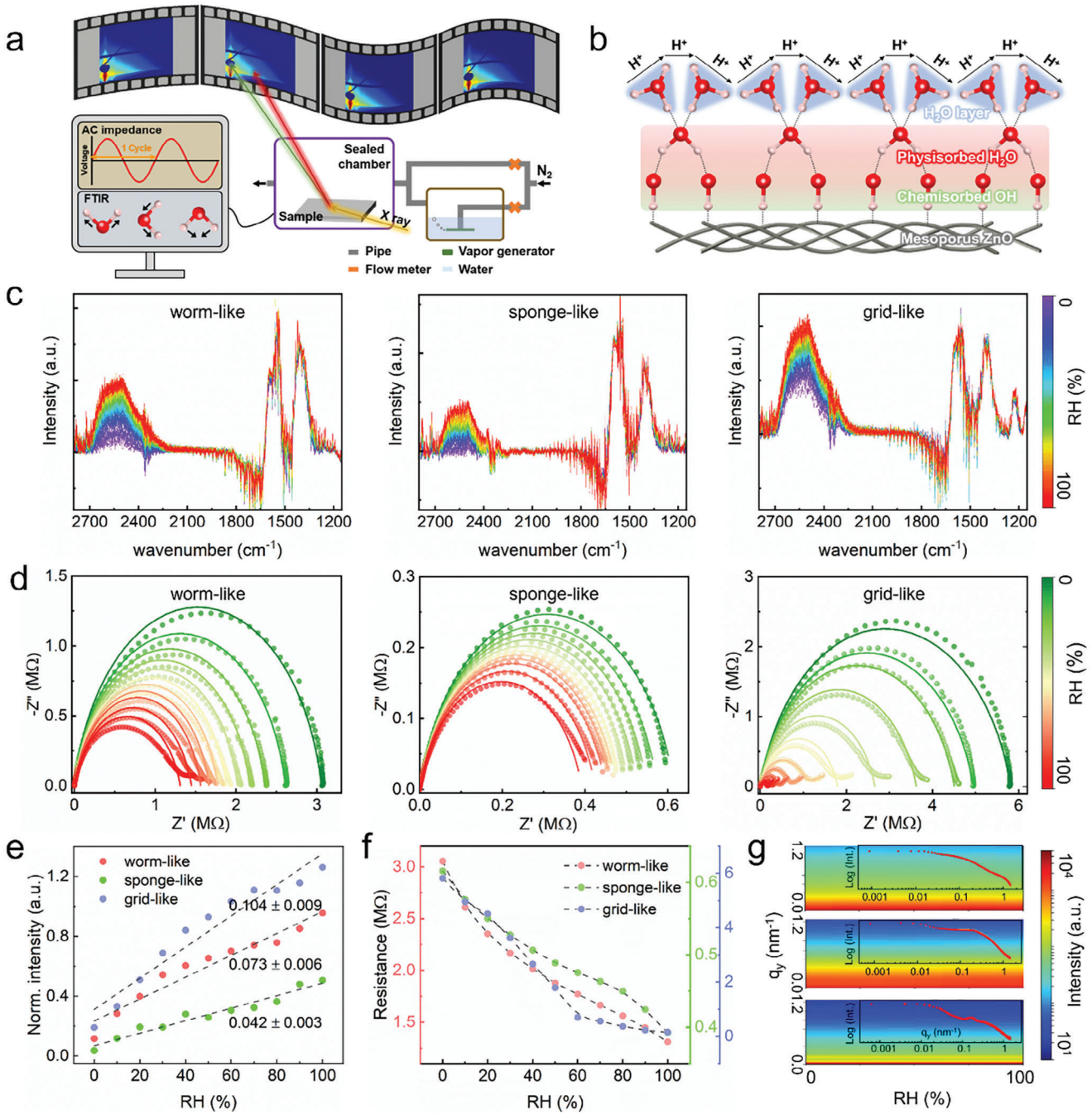

Figure 4. In situ investigations of the morphology-conductivity correlation during water adsorption. a) Schematic diagram of the in situ measurement setup for humidity-dependent FTIR, GISAXS, and AC impedance experiments. b) Schematic presentation of the interaction between water molecules and mesoporous ZnO films. c) In situ FTIR spectra of worm-like (left panel), sponge-like (middle panel), and grid-like (right panel) ZnO films. In the scale bar, purple, and red curves represent the minimum and maximum RH, respectively. (d) RH-dependent Nyquist plots of worm-like (left panel), sponge-like (middle panel), and grid-like (right panel) ZnO films. The scale bar represents the humidity levels, in which the green and red are for the minimum and maximum RH, respectively. e) Peak intensity of the D_2O band of mesoporous ZnO films. f) The corresponding R_f determined from the impedance spectra by equivalent circuit fit analysis. g) 2D mapping generated from the horizontal line cuts of in situ GISAXS data of worm-like (upper row), sponge-like (middle row) and grid-like (bottom row) ZnO films, showing a stable morphology during water adsorption. The insets are the integrated GISAXS data of horizontal line cuts as a function of increased humidity levels.

© 2023 The Authors. Advanced Functional Materials published by Wiley-VCH GmbH

observed for all mesoporous ZnO films. During the RH ramping, the D_2O vibration mode emerges at 2500 cm^{-1} and progressively increases with elevated RH levels, evidencing the high sensitivity of all ZnO films toward the water vapor. However, the H_2O vibration mode is observed to decrease at the same time, which is due to the deuteration of the ZnO films by D-H exchange.[54] The COO— remaining on the ZnO film can interact with water through the hydrogen bonds, from which we would thus expect a peak shift or broadening of this characteristic peak. However, no pronounced changes can be detected for two predominant characteristic peaks (1577 and 1385 cm^{-1}), signifying a negligible effect of COO— groups on water adsorption. In contrast, this verifies that ZnO represents the main factor contributing to water adsorption rather than the residuals. To quantify the water adsorption, the D_2O band (2500 cm^{-1}) is normalized to the most intense peak (1577 cm^{-1}) for each case. Consequently, we can evaluate the amount of D_2O bound to the respective ZnO film by tracking the relative intensity evolution of the D_2O peak. Apparently, all films show a monotonic increase in peak intensity with increased water exposure (Figure 4e). At any given RH value, the grid-like ZnO film shows the highest intensity, implying the highest adsorption capability by binding the most water molecules. By applying a linear fit, the slope of the curve can be determined, which is equivalent to the rate constant (k) quantifying the adsorption kinetics. Within the uncertainties, the k values of mesoporous ZnO films follow a decreasing tendency in the order of grid-like (0.104 ± .009), worm-like (0.073 ± 0.006) and sponge-like (0.042 ± 0.003). Therefore, we can conclude the water adsorption process is morphology-dependent, and the grid-like ZnO film is distinguished to be the most sensitive and has the fastest adsorption kinetics. The RH variation significantly impacts surface chemistry, consequently, modulating the electrical properties in mesoporous ZnO film. Figure 4d compares the Nyquist plots for three different kinds of mesoporous ZnO films from the lowest to the highest RH conditions. As indicated by the continuous narrowing of semicircles (for all films) and the emergence of straight lines (only for grid-like ZnO film at high RH) in the impedance spectra, all films show good electrical response over the entire humidity range. An equivalent circuit (EC) analysis is conducted to reveal the underlying conduction mechanism in more detail. At the minimum RH, the impedance spectra of all films are represented by semicircles, which are typical of a "non-Debye" behavior due to polarization.[55] To account for this, the commonly used EC can be described by the parallel connected resistor (R_f) and capacitor (C_f) (Figure S11a,b, Supporting Information). R_f and C_f denote the resistance and impedance of the film, respectively.[56] Correspondingly, an R_f of 3.05, 0. 62, and 5.82 MΩ for the worm-like, sponge-like, and grid-like ZnO film are determined, respectively (Figure 4f). Note that the conductivity of these mesoporous ZnO films is comparatively lower than that of the compact ZnO counterparts. This scenario can be mainly ascribed to the abundant presence of pores, which would exert a detrimental effect to some extent by impeding charge carrier transport.[57] The trend of R_f at the minimum RH coincides with that of the water-related characteristic signal observed in Figure S10 (Supporting Information). Thus, the differences in conduction behavior at the minimum humidity level can be interpreted by water adsorption. Considering the fact that the adsorption of water molecules on nanostructured ZnO would create a depletion region on the surface, the content of adsorbed molecules would vary the density and mobility of charge carriers.[57,58] Compared to the other two cases, the depletion depth in the grid-like ZnO film is suspected to be larger and hence, poorer electrical conduction. With increasing RH (>50% RH), an obvious short line emerges at the low-frequency region and coexists with the semicircles at the high-frequency range for the grid-like ZnO film, which makes it different from the worm-like and sponge-like ones in the conduction. To account for this phenomenon, a Warburg impedance (C_w) element is assembled into the EC by a series combination with the R-C parallel circuit mentioned above (Figure S11c,d, Supporting Information). Typically, C_w originates from the diffusion process of electroactive species (such as ions) at the interface between electrodes and the film.[59] In this EC, the contribution of C_w to impedance outweighs that of R_f, indicating that ion diffusion dominates the conduction in grid ZnO film at high humidity.[60] As presented in Figure 4f, a monotonic dependence of the R_f value on the RH level can be found for all mesoporous ZnO films. Nevertheless, these films still feature some differences from the viewpoint of the relative decrease in the magnitude of the R_f value in the specific RH range, which can be alternatively interpreted as humidity sensitivity. With RH increasing to 100% RH, the R_f can be approximated to linearly decrease to 1.31 and 0.39 MΩ for the worm-like and sponge-like ZnO film, respectively. However, two types of RH-dependent response behavior can be distinguished for the grid-like ZnO film. Within the 0–50% RH range, the R_f of grid-like ZnO film also shows an almost steady decreasing tendency from 5.82 to 1.78 MΩ. When reaching 60% RH, the R_f rapidly reduced to 0.70 MΩ, which is nearly one order of magnitude lower than that at 50% RH. Following this evolution, the R_f proceeds to decrease but at a slower rate. However, we do not observe any saturation point for the R_f even though the water flow rises to 100%, which can be reasonably interpreted by the maximum RH level the chamber can achieve in reality. When the RH reaches this value (≈80% RH), the lowest R_f obtained for grid-like ZnO film is 0.15 MΩ. To quantitatively describe the humidity sensitivity (RS), the relative values of $(R_{fmin}\text{-}R_{fmax})/R_{fmax}$ are estimated, where R_{fmin} and R_{fmax} represent the R_f values at the minimum and maximum RH levels, respectively. The humidity sensitivity improves with the order of sponge- (37%), worm- (57%), and grid-like ZnO (88%), consistent with the water adsorption capability indicated by in situ FTIR spectra.

Such a positive relationship between water uptake and film resistance can be attributed to the humidity-dependent conduction mechanism. Based on the previous report, the defects would endow ZnO structures with higher local charge density and a stronger electrostatic field, providing an advantageous effect for the dissociation of water molecules.[61] As we have discussed before, our calculation results also support this. When applying an external electric field to the mesoporous ZnO films, the dissociation of adsorbed water molecules would further occur and generate ionic (protonic) species, which would migrate and contribute to global conductivity. Protons, as the dominant charge carriers, may transfer from site to site across the mesoporous ZnO film surface via the hopping mechanism, accounting for the relatively high impedances at low RH.[62] Such a hopping transport often occurs through the chemisorbed water layer as illustrated in Figure 4b. Because the small amount of adsorbed water cannot fully cover the film surface, a proton can only be transported

© 2023 The Authors. Advanced Functional Materials published by Wiley-VCH GmbH

from an adsorbed OH group to a water molecule to generate H_3O^+. With increasing RH, more water molecules would be physisorbed onto the chemisorbed surface via the double hydrogen network and eventually give rise to a continuous water layer (Figure 4b), making electrolytic conduction possible and leading to an ionic current flow.[62,63] Such conduction coexists with the hopping transport but plays a dominant role. According to the ion transfer mechanism proposed by Grotthuss: $H_2O + H_3O^+ \rightarrow H_3O^+ + H_2O$, the energy barrier is small as the initial and final states are identical.[64] Therefore the H_3O^+ transfer within the physisorbed layer at high RH conditions would be much easier than the hopping at low RH, leading to a quick decrease in the impedance. With higher-level water vapor exposure, continuous physisorption on the ZnO surface would facilitate the formation of water multilayers and weaken the effect from the underlying chemisorbed layer. Hence, these physisorbed water multilayers would behave like a liquid, giving more freedom for the charge carriers for random movement. Moreover, the morphological differences play an important role in determining the humidity response sensitivity of the three mesoporous ZnO films by controlling the mass transfer pathway of the water molecules. As for the conductive differences among the mesoporous ZnO films, the grid-like one has the highest water adsorption capability and most interconnected 1D nanostructures, which facilitate the transfer of water to form the interaction region and enhance the charge carrier transport, especially at high RH conditions.

Having established that morphology plays an essential role in determining the water adsorption behavior and consequent electrical conductivity of mesoporous ZnO films, we turn back to monitoring the possible morphological changes during the water adsorption by in situ GISAXS. Figure 4g shows the corresponding 2D color mapping of horizontal line cuts extracted from the GISAXS data over the entire RH variation. The insets illustrate the superposed line cuts as a function of increased humidity levels, showing almost negligible changes across the whole scattering q range. Initially (at min 0% RH), the predominant scattering intensity concentrated in different q_y ranges is clearly visible, corresponding to the structural organization of mesoporous ZnO films at different spatial scales. According to the previous investigation, the water molecules cannot penetrate the ZnO crystal structure, meaning they can only be adsorbed onto the ZnO surface rather than adsorbed into the bulk of ZnO structure.[4] As potential radiation damage can be ruled out (Figure S12, Supporting Information) and X-rays achieve a high penetration depth, the scattering information collected reflects the average morphological characteristics of the entire ZnO film thickness plus the water molecular layers. Irrespective of humidity evolution, all mesoporous ZnO films are demonstrated to be morphologically stable as no distinguishable scattering change is detected over the entire length scales in the 2D mapping and corresponding 1D line cuts (Figure 4g). More details about selected 2D GISAXS data, 1D line cut profiles, and structural parameters of these mesoporous ZnO films are shown in Figures S13–S15 (Supporting Information). In each case, the selected 2D GISAXS data are almost identical, and all 1D line-cut profiles overlap pretty well without any discernible variations throughout the RH range. Based on the modeling results, only the large-sized domains exhibit slight fluctuations upon water adsorption regardless of the ZnO film morphology. In contrast, the other two characteristic structures remain mostly unaffected by this process. Considering the smallest volume contribution from the large-sized domains, the morphologies changes could thus be negligible. Accompanied by continuously enhanced water-related vibration signals observed in the in situ FTIR results, the substantially unchanged structural parameters in the in situ GISAXS data imply no straightforward correlation between the morphological features and water adsorption capability of the mesoporous ZnO films. This can also be rationalized by the fact that water adsorption only occurs at the defective ZnO surface, different from water absorption within the bulk of a hygroscopic film. With such good morphological stability, the mesoporous films hold great potential for humidity sensing materials toward further practical applications.

3. Conclusion

In summary, we have investigated the effect of water on mesoporous ZnO films by in situ monitoring the water adsorption, electrical properties, and morphology evolution. Attributed to the highly tailorable self-assembly behaviors using a block copolymer- assisted sol–gel synthesis strategy, three mesoporous ZnO films with varied structural dimensions and interconnectivity are obtained as model systems. As a consequence, both crystallinity and oxygen vacancy levels of the as-obtained ZnO films are identified to be morphology-dependent, in which the abundant presence of pores endows a weak crystalline nature but provides rich oxygen vacancies. Moreover, the theoretical calculations evidence that the presence of oxygen vacancies on the ZnO surface would further promote the adsorption and dissociation of the water molecules. Upon continued water vapor exposure with progressively elevated RH levels, all mesoporous ZnO films demonstrate pronounced water adsorption-dominated surface-chemistry behavior and highly moisture-dependent electrical response but superior morphological stability. Moreover, the morphology of mesoporous ZnO films is revealed as the dominant factor for water adsorption and consequent ion-modulated conductive property by enabling the ZnO films with different adsorption capabilities and transport pathways for charge carriers. The results shown for the grid-like ZnO film substantiate that the more ordered pore arrays residing within the interconnected ZnO networks play a vital role in water adsorption and consequent improvement in conductive properties, which could be exploited or suppressed depending on the types of practical applications. The morphology of mesoporous ZnO films can be additionally tailored by thermodynamic, kinetic factors, synthetic environments, or a combination of them, thus endowing different conductivity evolution that water molecules can modulate. The present work will shed light on the fundamental understanding of water-modulated mesoporous ZnO film surface chemistry and the resulting impact on electrical conductivity, which may pave the way for next-generation ZnO-involved electronic applications.

Supporting Information

Supporting Information is available from the Wiley Online Library or from the author.

© 2023 The Authors. Advanced Functional Materials published by Wiley-VCH GmbH

Acknowledgements

T.T., S.T., and A.X. contributed equally to this work. This work was supported by funding from the Deutsche Forschungsgemeinschaft (DFG, German Research Foundation) under Germany´s Excellence Strategy-EXC 2089/1-390776260 (e-conversion), TUM.solar in the context of the Bavarian Collaborative Research Project Solar Technologies Go Hybrid (SolTech), the Center for NanoScience (CeNS) and the International Research Training Group 2022 Alberta/Technical University of Munich International Graduate School for Environmentally Responsible Functional Hybrid Materials (ATUMS). The financial support from the China Scholarship Council (CSC) is also acknowledged. The authors thank Prof. Alexander Holleitner for providing access to the SEM measurements. The authors acknowledge the CERIC-ERIC Consortium for access to the Austrian SAXS beamline.

Open access funding enabled and organized by Projekt DEAL.

Conflict of Interest

The authors declare no conflict of interest.

Data Availability Statement

The data that support the findings of this study are available from the corresponding author upon reasonable request.

Keywords

in situ, mesoporous ZnO film, morphology-property relationship, self-assembly, water adsorption

Received: September 26, 2023
Revised: October 22, 2023
Published online: November 5, 2023

[1] a) Z. W. Pan, Z. R. Dai, Z. L. Wang, *Science* **2001**, *291*, 1947; b) Z. L. Wang, *Adv. Mater.* **2003**, *15*, 432; c) S. Xu, Z. L. Wang, *Nano Res.* **2011**, *4*, 1013; d) H. Zeng, X. Xu, Y. Bando, U. K. Gautam, T. Zhai, X. Fang, B. Liu, D. Golberg, *Adv. Funct. Mater.* **2009**, *19*, 3165.
[2] a) T. W. Hamann, A. B. F. Martinson, J. W. Elam, M. J. Pellin, J. T. Hupp, *Adv. Mater.* **2008**, *20*, 1560; b) X. Zhou, Y. Zhu, W. Luo, Y. Ren, P. Xu, A. A. Elzatahry, X. Cheng, A. Alghamdi, Y. Deng, D. Zhao, *J. Mater. Chem. A* **2016**, *4*, 15064.
[3] a) E. Kim, Y. Vaynzof, A. Sepe, S. Guldin, M. Scherer, P. Cunha, S. V. Roth, U. Steiner, *Adv. Funct. Mater.* **2014**, *24*, 863; b) P. Zhang, J. Wu, T. Zhang, Y. Wang, D. Liu, H. Chen, L. Ji, C. Liu, W. Ahmad, Z. D. Chen, S. Li, *Adv. Mater.* **2018**, *30*, 1703737.
[4] G. Milano, M. Luebben, M. Laurenti, S. Porro, K. Bejtka, S. Bianco, U. Breuer, L. Boarino, I. Valov, C. Ricciardi, *Adv. Mater. Interfaces* **2019**, *6*, 1900803.
[5] K. Sarkar, M. Rawolle, E. M. Herzig, W. Wang, A. Buffet, S. V. Roth, P. Müller-Buschbaum, *ChemSusChem* **2013**, *6*, 1414.
[6] a) M. Lazzari, M. A. López-Quintela, *Adv. Mater.* **2003**, *15*, 1583; b) Y. Mai, A. Eisenberg, *Chem. Soc. Rev.* **2012**, *41*, 5969.
[7] a) L. Zu, X. Qian, S. Zhao, Q. Liang, Y. E. Chen, M. Liu, B.-J. Su, K.-H. Wu, L. Qu, L. Duan, H. Zhan, J.-Y. Zhang, C. Li, W. Li, J. Y. Juang, J. Zhu, D. Li, A. Yu, D. Zhao, *J. Am. Chem. Soc.* **2022**, *144*, 2208; b) S. Kim, J. Hwang, J. Lee, J. Lee, *Sci. Adv.* **2020**, *6*, eabb3814.
[8] W. Li, Q. Yue, Y. Deng, D. Zhao, *Adv. Mater.* **2013**, *25*, 5129.
[9] a) L. Song, W. Wang, S. Pröller, D. Moseguí González, J. Schlipf, C. J. Schaffer, K. Peters, E. M. Herzig, S. Bernstorff, T. Bein, D. Fattakhova-Rohlfing, P. Müller-Buschbaum, *ACS Energy Lett.* **2017**, *2*, 991; b) Y.-J. Cheng, J. S. Gutmann, *J. Am. Chem. Soc.* **2006**, *128*, 4658.
[10] a) S. Yu, H. Zhang, J. Zhang, Z. Li, *Sensors* **2019**, *19*, 5267; b) S. P. Gupta, A. S. Pawbake, B. R. Sathe, D. J. Late, P. S. Walke, *Sens. Actuators, B* **2019**, *293*, 83.
[11] R. Kumar, O. Al-Dossary, G. Kumar, A. Umar, *Nano Micro Lett* **2015**, *7*, 97.
[12] C.-Y. Chen, J. R. D. Retamal, I.-W. Wu, D.-H. Lien, M.-W. Chen, Y. Ding, Y.-L. Chueh, C.-I. Wu, J.-H. He, *ACS Nano* **2012**, *6*, 9366.
[13] a) X. Liu, Z. Zheng, J. Wang, Y. Wang, B. Xu, S. Zhang, J. Hou, *Adv. Mater.* **2022**, *34*, 2106453; b) Z. R. Tian, J. A. Voigt, J. Liu, B. Mckenzie, M. J. Mcdermott, M. A. Rodriguez, H. Konishi, H. Xu, *Nat. Mater.* **2003**, *2*, 821; c) J. Xu, Z. Chen, J. A. Zapien, C.-S. Lee, W. Zhang, *Adv. Mater.* **2014**, *26*, 5337.
[14] a) Y. Jiang, L. Sun, F. Jiang, C. Xie, L. Hu, X. Dong, F. Qin, T. Liu, L. Hu, X. Jiang, Y. Zhou, *Mater. Horiz.* **2019**, *6*, 1438; b) E. S. Jang, J.-H. Won, S.-J. Hwang, J.-H. Choy, *Adv. Mater.* **2006**, *18*, 3309.
[15] O. Dulub, B. Meyer, U. Diebold, *Phys. Rev. Lett.* **2005**, *95*, 136101.
[16] M. A. Henderson, *Surf. Sci. Rep.* **2002**, *46*, 1.
[17] a) J. T. Newberg, C. Goodwin, C. Arble, Y. Khalifa, J. A. Boscoboinik, S. Rani, *J. Phys. Chem. B* **2018**, *122*, 472; b) H. Shi, H. Yuan, Y. Sun, X. Ma, Z. Li, D. Zhou, Z. Li, X. Shao, *Nano Lett.* **2021**, *21*, 9567; c) B. Meyer, D. Marx, O. Dulub, U. Diebold, M. Kunat, D. Langenberg, C. Wöll, *Angew. Chem., Int. Ed.* **2004**, *43*, 6641.
[18] P. Müller-Buschbaum, *Adv. Mater.* **2014**, *26*, 7692.
[19] R. Mäki-Ontto, K. De Moel, W. De Odorico, J. Ruokolainen, M. Stamm, G. Ten Brinke, O. Ikkala, G. ten Brinke, O. Ikkala, *Adv. Mater.* **2001**, *13*, 117.
[20] M. Schwartzkopf, G. Santoro, C. J. Brett, A. Rothkirch, O. Polonskyi, A. Hinz, E. Metwalli, Y. Yao, T. Strunskus, F. Faupel, P. Müller-Buschbaum, S. V. Roth, *ACS Appl. Mater. Interfaces* **2015**, *7*, 13547.
[21] Y. Yoneda, *Phys. Rev.* **1963**, *131*, 2010.
[22] A. Hexemer, P. Müller-Buschbaum, *IUCrJ* **2015**, *2*, 106.
[23] P. Müller-Buschbaum, *Anal. Bioanal. Chem.* **2003**, *376*, 3.
[24] A. L. Oechsle, J. E. Heger, N. Li, S. Yin, S. Bernstorff, P. Müller-Buschbaum, *ACS Appl. Mater. Interfaces* **2022**, *14*, 30802.
[25] W. Wang, H. Liu, M. Mu, H. Yin, Y. Feng, *Polym. Chem.* **2015**, *6*, 2900.
[26] L. Znaidi, *Mater. Sci. Eng., B* **2010**, *174*, 18.
[27] C. Li, Q. Li, Y. V. Kaneti, D. Hou, Y. Yamauchi, Y. Mai, *Chem. Soc. Rev.* **2020**, *49*, 4681.
[28] J. Ruokolainen, J. Tanner, G. Ten Brinke, O. Ikkala, M. Torkkeli, R. Serimaa, *Macromolecules* **1995**, *28*, 7779.
[29] a) D. Dong, T. Wang, Y. Sun, J. Fan, Y.-C. Lu, *Nature Sustain* **2023**, 1; b) C. E. Sing, J. W. Zwanikken, M. Olvera De La Cruz, *Nat. Mater.* **2014**, *13*, 694.
[30] Y. Ren, Y. Zou, Y. Liu, X. Zhou, J. Ma, D. Zhao, G. Wei, Y. Ai, S. Xi, Y. Deng, *Nat. Mater.* **2020**, *19*, 203.
[31] Z. Jiang, *J. Appl. Crystallogr.* **2015**, *48*, 917.
[32] P. Yang, D. Zhao, D. I. Margolese, B. F. Chmelka, G. D. Stucky, *Nature* **1998**, *396*, 152.
[33] Y. Qiu, S. Yang, *Adv. Funct. Mater.* **2007**, *17*, 1345.
[34] A. Mclaren, T. Valdes-Solis, G. Li, S. C. Tsang, *J. Am. Chem. Soc.* **2009**, *131*, 12540.
[35] M.-H. Jung, M.-J. Chu, *J. Mater. Chem. C* **2014**, *2*, 6675.
[36] a) S. Tu, T. Tian, A. Lena Oechsle, S. Yin, X. Jiang, W. Cao, N. Li, M. A. Scheel, L. K. Reb, S. Hou, A. S. Bandarenka, M. Schwartzkopf, S. V. Roth, P. Müller-Buschbaum, *Chem. Eng. J.* **2022**, *429*, 132295; b) J. Rivnay, S. C. B. Mannsfeld, C. E. Miller, A. Salleo, M. F. Toney, *Chem. Rev.* **2012**, *112*, 5488.
[37] D. P. Mcmeekin, P. Holzhey, S. O. Fürer, S. P. Harvey, L. T. Schelhas, J. M. Ball, S. Mahesh, S. Seo, N. Hawkins, J. Lu, M. B. Johnston, J. J. Berry, U. Bach, H. J. Snaith, *Nat. Mater.* **2023**, *22*, 73.

© 2023 The Authors. Advanced Functional Materials published by Wiley-VCH GmbH

[38] a) X. Song, K. Zhang, R. Guo, K. Sun, Z. Zhou, S. Huang, L. Huber, M. Reus, J. Zhou, M. Schwartzkopf, S. V. Roth, W. Liu, Y. Liu, W. Zhu, P. Müller-Buschbaum, *Adv. Mater.* **2022**, *34*, 2200907; b) A. Z. Chen, M. Shiu, J. H. Ma, M. R. Alpert, D. Zhang, B. J. Foley, D.-M. Smilgies, S.-H. Lee, J. J. Choi, *Nat. Commun.* **2018**, *9*, 1336.
[39] C. Sripan, V. E. Madhavan, A. K. Viswanath, R. Ganesan, *Mater. Lett.* **2017**, *189*, 110.
[40] S. Gandla, S. R. Gollu, R. Sharma, V. Sarangi, D. Gupta, *Appl. Phys. Lett.* **2015**, *107*, 152102.
[41] a) C.-M. Jiang, L. I. Wagner, M. K. Horton, J. Eichhorn, T. Rieth, V. F. Kunzelmann, M. Kraut, Y. Li, K. A. Persson, I. D. Sharp, *Mater. Horiz.* **2021**, *8*, 1744; b) H. Idriss, *Surf. Sci.* **2021**, *712*, 121894.
[42] G. Milano, L. D'ortenzi, K. Bejtka, L. Mandrile, A. M. Giovannozzi, L. Boarino, C. F. Pirri, C. Ricciardi, S. Porro, *J. Phys. Chem. C* **2018**, *122*, 8011.
[43] J. Wang, R. Chen, L. Xiang, S. Komarneni, *Ceram. Int.* **2018**, *44*, 7357.
[44] a) V. Srikant, D. R. Clarke, *J. Appl. Phys.* **1998**, *83*, 5447; b) Z. L. Wang, *ACS Nano* **2008**, *2*, 1987.
[45] a) P. Nagpal, V. I. Klimov, *Nat. Commun.* **2011**, *2*, 486; b) J. Eichhorn, S. P. Lechner, C.-M. Jiang, G. Folchi Heunecke, F. Munnik, I. D. Sharp, *J. Mater. Chem. A* **2021**, *9*, 20653.
[46] H. Razavi-Khosroshahi, K. Edalati, J. Wu, Y. Nakashima, M. Arita, Y. Ikoma, M. Sadakiyo, Y. Inagaki, A. Staykov, M. Yamauchi, Z. Horita, M. Fuji, *J. Mater. Chem. A* **2017**, *5*, 20298.
[47] L. Saikia, D. Bhuyan, M. Saikia, B. Malakar, D. K. Dutta, P. Sengupta, *Appl. Catal., A* **2015**, *490*, 42.
[48] P. E. Blöchl, *Phys. Rev. B* **1994**, *50*, 17953.
[49] R. Schaub, P. Thostrup, N. Lopez, E. Lægsgaard, I. Stensgaard, J. K. Nørskov, F. Besenbacher, *Phys. Rev. Lett.* **2001**, *87*, 266104.
[50] a) J. Zhang, D. Leng, L. Zhang, G. Li, F. Ma, J. Gao, H. Lu, B. Zhu, *J. Alloys Compd.* **2021**, *853*, 157339; b) K.-S. Chou, T.-K. Lee, F.-J. Liu, *Sens. Actuators, B* **1999**, *56*, 106.
[51] Y. Rong, Z. Tang, Y. Zhao, X. Zhong, S. Venkatesan, H. Graham, M. Patton, Y. Jing, A. M. Guloy, Y. Yao, *Nanoscale* **2015**, *7*, 10595.
[52] a) Q. Sun, *Vib. Spectrosc.* **2009**, *51*, 213; b) R. Vyumvuhore, A. Tfayli, H. Duplan, A. Delalleau, M. Manfait, A. Baillet-Guffroy, *Analyst* **2013**, *138*, 4103.
[53] M. Montero-Muñoz, J. E. Ramos-Ibarra, J. E. Rodríguez-Páez, M. D. Teodoro, G. E. Marques, A. R. Sanabria, P. C. Cajas, C. A. Páez, B. Heinrichs, J. A. H. Coaquira, *Appl. Surf. Sci.* **2018**, *448*, 646.
[54] L. P. Kreuzer, T. Widmann, N. Hohn, K. Wang, L. Bießmann, L. Peis, J.-F. Moulin, V. Hildebrand, A. Laschewsky, C. M. Papadakis, P. Müller-Buschbaum, *Macromolecules* **2019**, *52*, 3486.
[55] Q. Qi, T. Zhang, Q. Yu, R. Wang, Y. Zeng, L. Liu, H. Yang, *Sens. Actuators, B* **2008**, *133*, 638.
[56] A. R. C. Bredar, A. L. Chown, A. R. Burton, B. H. Farnum, *ACS Appl. Energy Mater.* **2020**, *3*, 66.
[57] H. He, Y. Fu, W. Zang, Q. Wang, L. Xing, Y. Zhang, X. Xue, *Nano Energy* **2017**, *31*, 37.
[58] S. Niu, Y. Hu, X. Wen, Y. Zhou, F. Zhang, L. Lin, S. Wang, Z. L. Wang, *Adv. Mater.* **2013**, *25*, 3701.
[59] C.-D. Feng, S.-L. Sun, H. Wang, C. U. Segre, J. R. Stetter, *Sens. Actuators, B* **1997**, *40*, 217.
[60] W. Geng, Q. Yuan, X. Jiang, J. Tu, L. Duan, J. Gu, Q. Zhang, *Sens. Actuators, B* **2012**, *174*, 513.
[61] J. H. Anderson, G. A. Parks, *J. Phys. Chem.* **1968**, *72*, 3662.
[62] B. M. Kulwicki, *J. Am. Ceram. Soc.* **1991**, *74*, 697.
[63] R. Wang, X. Liu, Y. He, Q. Yuan, X. Li, G. Lu, T. Zhang, *Sens. Actuators, B* **2010**, *145*, 386.
[64] F. M. Ernsberger, *J. Am. Ceram. Soc.* **1983**, *66*, 747.

© 2023 The Authors. Advanced Functional Materials published by Wiley-VCH GmbH